Polar amplification as a preferred response in an idealized aquaplanet GCM

Peter L. Langen

Ice and Climate Research

Niels Bohr Institute, University of Copenhagen, Copenhagen, Denmark

and

Vladimir A. Alexeev

International Arctic Research Center

University of Alaska Fairbanks, Fairbanks, Alaska, USA

Original published in *Climate Dynamics (2007), 29:305-317*

DOI 10.1007/s00382-006-0221-x

Corresponding author:

Peter L. Langen (plangen@gfy.ku.dk)

Ice and Climate Research, Niels Bohr Institute, University of Copenhagen

Juliane Maries Vej 30

DK-2100 Copenhagen O, Denmark

Abstract

An aquaplanet atmospheric general circulation model (GCM) coupled to a mixed layer ocean is analyzed in terms of its polar amplified surface temperature response to a $2\times CO_2$-like steady forcing and in terms of the phase space trajectory of the relaxation of a free perturbation to equilibrium. In earlier studies concerned with linear stability analysis of the same system we have shown that the least stable mode of the linearized surface budget operator has a polar amplified shape. We demonstrate that this shape of the least stable mode is responsible for the polar amplified shape of the response to a uniform forcing and for the manner in which the system relaxes back to equilibrium. Based on GCM and simple energy balance model results it is argued that the decay time-scale of this mode is determined by the sensitivity of the net top-of-atmosphere radiation to surface temperature while its shape (and thus the degree of polar amplification in a climate change experiment) is determined by the sensitivity of poleward heat transports to low- and high-latitude temperatures by the faster time-scale atmospheric dynamics. This implies that the underlying mechanisms for the polar amplification may be obscured when studying feedbacks during the slow evolution of climate change or considering only the new equilibrium state after introduction of a steady forcing.

1 Introduction

When the climate cools or warms, high latitude regions tend to exaggerate the changes seen at lower latitudes. This effect is called polar amplification and is seen in model projections of future climate (e.g., ACIA, 2004; Holland and Bitz, 2003) and, in fact, in the very earliest simple model of CO_2-induced climate change (Arrhenius, 1896). Polar amplification is found in proxy-records of both deep past warm periods (e.g., Zachos et al., 2001) and of the more recent cold glacials (e.g., Masson-Delmotte et al., 2006).

The surface albedo feedback (SAF), by which a warming leads to snow and ice

melt and thus greater absorption of solar energy, plays a role in producing polar amplified climate response and variability (e.g., Hall, 2004), and has therefore received close attention in recent years (e.g., Qu and Hall, 2006; Hall and Qu, 2006). By analyzing the output of twelve IPCC Fourth Assessment Report GCMs, however, Winton (2006) has recently proposed that the SAF does not dominate the simulated polar amplification; longwave effects appear to play an equally important role. Even with the SAF excluded, several GCM studies (Schneider et al., 1999; Alexeev, 2003; Alexeev et al., 2005) have found feedbacks involving increased longwave forcing on the high-latitude surface temperature sufficient to amplify high-latitude temperatures to much the same degree as with the SAF included.

Alexeev et al. (2005) found that a low-latitude warming increases the poleward atmospheric heat and moisture transport leading to a warmer and more moist high-latitude atmosphere. This, in turn, warms the surface through increased longwave forcing. This mechanism is in agreement with the recent findings of Solomon (2006) whereby the coherence between developing storms and latent heat release contributes significantly to polar warming through increased dynamical heat transports. Several other investigators have noted the potential for low-latitude warming to influence the high-latitude longwave forcing (Schneider et al., 1997; Rodgers et al., 2003), although the idea of a low-latitude thermal forcing being felt at high-latititudes is not new; the existence atmospheric teleconnection patterns has, for example, been known for about 25 years (e.g., Wallace and Gutzler, 1981; Hoskins and Karoly, 1981).

Cai (2005, 2006) has investigated the interactions between increased dynamical heat transports and the longwave radiation field in a box model of the surface and the atmosphere. In this model, the climate system is represented by two surface boxes and two atmospheric boxes, and an increase in atmospheric emissivity (greenhouse forcing) is found to increase the meridional temperature gradient in the atmosphere and thereby the heat transport. In agreement with the proposal of Alexeev et al. (2005), this decreases the longwave forcing at low latitudes, increases it at high

latitudes and eventually leads to polar amplification.

In a CO_2-doubling experiment with the CCC GCM coupled to a mixed-layer ocean, Boer (1995) found a polar amplified surface temperature response accompanied by a very modest change in total poleward atmospheric energy transport. The small change was found to occur due to a cancellation between a decrease in dry static energy transport and an increase in the latent heat transport due to increased moisture supply from the warming low latitudes. A similar cancellation will be shown to be at the heart of the findings in the present study. The importance of increased latent heat transport relative to that of the SAF for high-latitude warming was noted already by Manabe and Wetherald (1980). This study also showed that the climatic response to CO_2 and solar constant changes have almost identical meridional structures although the forcings are rather different. This will in the framework of the present study be interpreted as an excitation of a certain mode in the system. In Alexeev (2003) and Langen and Alexeev (2005) it was demonstrated how the meridional structure of a climate response resembles that of the least stable mode of the linear surface budget operator of the system. This idea will be investigated further here; in particular, we will determine the physical meanings of the slowest decaying (i.e., least stable) mode and faster decaying modes and the parameters controlling their shapes and time-scales.

According to Alexeev (2003), Shine et al. (2003) and Hansen et al. (2006), an adjusted troposphere-stratosphere forcing (holding surface temperatures or at least SSTs constant) performs better than the typical stratosphere-only-adjusted forcing in predicting the eventual surface temperature change resulting from a change in a forcing agent. When changing an agent and letting the troposphere and stratosphere equilibrate with fixed SSTs, the global-average imbalance (i.e., the forcing) will be the same at all levels in the atmosphere. Its geographical distribution, however, will depend on the level, and Alexeev (2003) demonstrated the surface-approach to be efficient in characterizing the forcing-response relationship in the geographical sense and not only the global-average sense. The linear theory employed in the following

builds on an assumption of the local SST depending on the local surface budget depending, in turn, on the global distribution of SSTs. The top-of-atmosphere (TOA) budget does depend only (with the assumptions made here) on the distribution of SSTs, but this budget does not as directly control the local SSTs. For this reason, we have chosen to continue with the surface-approach rather than using the more standard TOA approach.

In Section 2 we will present the experimental configuration of the GCM employed in the study and review the linear framework for interpreting the GCM's dynamics. Section 3 describes a two-box energy balance model designed to clearly express the physics of the system's modes and their time-scales. In Section 4 these findings are compared with the behavior of the GCM in an ensemble run and conclusions are offered in Section 5.

2 Linear dynamics of a simplified GCM

In previous papers (Alexeev, 2003; Langen and Alexeev, 2005) we have described several ways of determining a linearized surface budget operator of a climate system model. For the sake of completeness, and since this is essential to the present paper, we will here review the ideas of the linearized surface budget. Firstly, however, we will describe the simplified GCM configuration used in the experiments throughout this study.

2.1 Experimental configuration

In this study we use the National Center for Atmospheric Research's CCM3 atmospheric general circulation model (Kiehl et al., 1996) in a special simplified configuration. The model has 18 vertical levels and we employ a horizontal spectral resolution of T21. Continents have been removed from the model geography leaving us with a so-called aquaplanet, and sea ice effects have been excluded by treating sub-freezing grid points as open water in the model code. A 50 m deep mixed

layer ocean model (or slab ocean) with a weak, specified deep ocean heat flux convergence ("q-flux", as described by Langen and Alexeev (2004)) acts as the lower boundary condition for the atmospheric model. By employing what we call modified equinox forcing (Alexeev, 2003), whereby an annual average diurnal cycle provides the same solar forcing every model day, we have removed the seasonal cycle. The solar constant and the CO_2 concentration are specified at 1367 Wm^{-2} and 355 ppm, respectively. The surface albedo is uniform and fixed (at 11%) and has been tuned along with the strength of the specified q-flux to produce a global mean temperature and equator-to-pole temperature gradient similar to those of the present day climate.

These simplifications render the model climate particularly well suited for the idealized investigations carried out here. The statistics of the climate have no seasonal cycle (symmetry in time), no standing waves (zonal symmetry) and no differences between the hemispheres (hemispherical symmetry). Due to these properties we will mainly concern ourselves with zonally averaged quantities throughout the study.

2.2 Linearized surface budget

The temperature of the oceanic mixed layer is in the model code governed by the budget of the surface fluxes,

$$\rho_w c_w H \frac{\partial \mathbf{T}_S}{\partial t} = \mathbf{F}_S - \mathbf{F}_L - \mathbf{F}_{SH} - \mathbf{F}_{LH} + \mathbf{Q}, \tag{1}$$

where $\mathbf{F}_S$ is the net downwelling shortwave flux, $\mathbf{F}_L$ is the net upwelling longwave flux, and $\mathbf{F}_{SH}$ and $\mathbf{F}_{LH}$ are the net upwelling fluxes of sensible and latent heat. The heat capacity per unit area of the mixed layer is given by the product of the density of sea water, ρ_w, the specific heat capacity, c_w, and the depth, H, and will in the following be written simply as c. $\mathbf{Q}$ resembles the contribution to the budget from the oceanic heat flux convergence, but since this quantity is kept fixed throughout the experiments, it drops out once we consider linearizations about an equilibrium.

Note that the temperature and the fluxes are written in a bold font to signify that they are vectors; in principle they could be vectors of all the points on the surface of the globe, but here we will think of them just as vectors of the zonal average quantities. During model integration, however, eqn. (1) holds locally. This differs from the integrations by Alexeev (2003) where the SSTs at each time-step were constrained to be zonally symmetric.

With our 50 m mixed-layer depth, the typical time-scale for atmospheric response is significantly shorter than that for the ocean, and the atmospheric time-scale can be regarded as negligible compared to the longer oceanic time-scales. Since the atmosphere is chiefly heated from below, the atmospheric state averaged over the short atmospheric time-scales will be given by the state of the ocean. Even in a situation where the ocean is not in equilibrium with its surface fluxes, the atmosphere will spin up to match this state such that (on the short time average) the fluxes in and out of the bottom and top of the atmosphere balance. The atmosphere can thus be regarded as being in quasi-equilibrium with the SSTs and we will assume that to a given state of the SST field corresponds a given mean state of the atmosphere and a given set of surface fluxes. In the following analysis we will thus approximate eqn. (1) by

$$\dot{\mathbf{T}}_S \simeq c^{-1}\ \mathbf{B}_{Srf}(\mathbf{T}_S, \mathbf{\Lambda}), \tag{2}$$

where $\mathbf{B}_{Srf}$ is the net surface flux and $\mathbf{\Lambda}$ is a collection of parameters, such as the CO_2 concentration and the solar constant, external to the system, in the sense that they are not influenced by the state of the system. The quantities $\mathbf{T}_S$ and $\mathbf{B}_{Srf}$ should be thought of as averages over the short time-scales (say, 50–100 days) that allow us to regard the atmosphere as being determined by the state of the SSTs. $\mathbf{B}_{Srf}$ will thus be assumed to depend only on the SSTs and the external parameters.

Integration of the GCM from random initial conditions (not shown) indicates that the dynamical system described by eqn. (2) is stable: after an initial transient, the system eventually fluctuates around an equilibrium state. Letting overbars de-

note time-averages on the long oceanic time-scale and performing this operation on eqn. (2), we get

$$\dot{\bar{\mathbf{T}}}_S = c^{-1}\ \mathbf{B}_{Srf}(\bar{\mathbf{T}}_S, \mathbf{\Lambda}) \simeq \mathbf{0} \tag{3}$$

since the system otherwise would drift away from the equilibrium. Expanding eqn. (2) to first order in $\mathbf{T}'_S = \mathbf{T}_S - \bar{\mathbf{T}}_S$ we get

$$\dot{\mathbf{T}}'_S = c^{-1}\ \mathbf{B}_{Srf}(\bar{\mathbf{T}}_S + \mathbf{T}'_S, \mathbf{\Lambda}) \simeq c^{-1}\ \boldsymbol{\mathcal{R}}(\bar{\mathbf{T}}_S)\ \mathbf{T}'_S, \tag{4}$$

where $\boldsymbol{\mathcal{R}}$ is the Jacobian of the surface budget with respect to the SSTs (evaluated at equilibrium),

$$\boldsymbol{\mathcal{R}}(\bar{\mathbf{T}}_S) = \left.\frac{D\mathbf{B}_{Srf}(\mathbf{T}_S, \mathbf{\Lambda})}{D\mathbf{T}_S}\right|_{\mathbf{T}_S = \bar{\mathbf{T}}_S}. \tag{5}$$

The eigenvalues and eigenvectors of the matrix of a linear dynamical system such as eqn. (4) provide full information about the system in terms of decay of free perturbations and responses to steady forcings. As will be demonstrated in the following, especially the eigenvector of $\boldsymbol{\mathcal{R}}$ associated with the smallest eigenvalue (in terms of magnitude), i.e., the least stable mode, is worth closer examination.

2.3 Decay of free perturbations

Since the above equilibrium is stable in both the GCM and its linearized approximation, eqn. (4), the real parts of all the eigenvalues of $\boldsymbol{\mathcal{R}}$ are negative and the manner in which the system removes a perturbation in the surface temperature field can be seen from the solution of eqn. (4),

$$\mathbf{T}'_S(t) = k_1\mathbf{v}_1 e^{\lambda_1 t} + \ldots + k_N\mathbf{v}_N e^{\lambda_N t}, \tag{6}$$

where the λ's are the eigenvalues and the k's give the initial perturbation in the basis of the eigenvectors. With negative real parts of the eigenvalues, all the terms in the expansion will decay exponentially (with an e-folding time of $-1/Re(\lambda)$). When all

but the slowest decaying term in the expansion have decayed, the final approach of the system toward equilibrium is along the least stable mode (LSM).

The degree to which the LSM will stand out during the final approach to equilibrium is determined by the separation in time-scales of the LSM from the other modes. In previous papers we have employed different ways of evaluating $\boldsymbol{\mathcal{R}}$; in Alexeev (2003) a perturbation method was used and in Langen and Alexeev (2005) the statistics of an unforced control run were exploited using the fluctuation-dissipation theorem (FDT). In both cases, the smallest eigenvalue corresponded to a time-scale about 5 times longer than that of the second smallest. The LSM associated with this eigenvalue was for both methods a typical polar amplified pattern and with the GCM used in the present study, the perturbation method yields a time-scale of 125 months (and 55 months with a different GCM, Alexeev, 2003) while the FDT method gives 90 months. Hence, if we pull the system away from equilibrium and let it relax freely, it will, after the faster modes have decayed, approach equilibrium along a direction in phase space corresponding to the polar amplified pattern. This will be demonstrated to be the case in Section 4.

2.4 Response to steady forcing

A different experiment is one where we apply a steady forcing to the surface budget. This could for example be due to a doubling of CO_2 or a change in the solar constant, but here we will write it formally as $\Lambda \rightarrow \Lambda + \delta\Lambda$. This change in the external parameters leads to a change in the surface forcing of

$$\delta \mathbf{b} \simeq \frac{\partial \mathbf{B}_{Srf}(\bar{\mathbf{T}}_S, \Lambda)}{\partial \Lambda} \delta\Lambda, \tag{7}$$

averaged over the short atmospheric time-scale without oceanic response. After an equilibration period, the system will eventually come close to a new equilibrium,

$\bar{\mathbf{T}}_S + \delta\mathbf{T}_S$, in which

$$\mathbf{B}_{Srf}(\bar{\mathbf{T}}_S + \delta\mathbf{T}_S, \Lambda + \delta\Lambda) \simeq \boldsymbol{\mathcal{R}}\delta\mathbf{T}_S + \delta\mathbf{b}. \tag{8}$$

Since we are in a new equilibrium, this surface budget will vanish and we can solve for the surface temperature change

$$\delta\mathbf{T}_S = -\boldsymbol{\mathcal{R}}^{-1}\delta\mathbf{b}. \tag{9}$$

Hence, if we evaluate the Jacobian (e.g., as in Alexeev, 2003; Langen and Alexeev, 2005), we will be able to calculate the linear estimate of the climate change arising from any surface forcing. Moreover, in the case where we have real eigenvalues and a complete set of eigenvectors, we may expand the forcing in the basis of these eigenvectors to get (Alexeev, 2003),

$$\begin{aligned} \delta\mathbf{T} &= -\boldsymbol{\mathcal{R}}^{-1}\delta\mathbf{b} = -\boldsymbol{\mathcal{R}}^{-1}\sum_i b_i\mathbf{v}_i \\ &= -\sum_i b_i\boldsymbol{\mathcal{R}}^{-1}\mathbf{v}_i \underbrace{=}_{1} -\sum_i \frac{b_i}{\lambda_i}\mathbf{v}_i \\ &\underbrace{\simeq}_{2} -\frac{b_l}{\lambda_l}\mathbf{v}_l, \end{aligned} \tag{10}$$

where the b's are the projection coefficients of the forcing onto the eigenvectors. Here, equality 1 is due to the eigenvectors of $\boldsymbol{\mathcal{R}}$ also being eigenvectors of $\boldsymbol{\mathcal{R}}^{-1}$ and the approximate equality 2 holds if the l'th term dominates the expansion. This is the case if the forcing projects similarly onto the eigenvectors and the l'th eigenvalue is much smaller than the others, i.e., if the LSM is well separated from the other modes. If this is satisfied, we have found that the shape of climate change is given by the shape of the least stable mode. This can, in fact, be shown also to hold in the case of complex eigenvalues if one mode has $|\lambda|$ smaller and well separated from the others.

Hence, if the forcing projects significantly onto the least stable mode, the climate

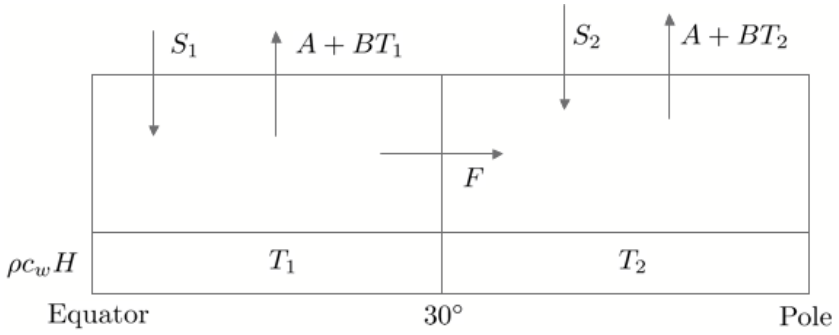

Figure 1: Sketch of the two-box EBM. The ocean mixed layer has in both boxes a depth of H, density ρ, and specific heat capacity c_w. The surface (and mixed layer) temperatures in the boxes are T_1 and T_2 and the net downwelling shortwave radiations are S_1 and S_2. The outgoing longwave radiations are parameterized as $A + BT_i$ and the heat transport from box 1 to box 2 is F.

change will be given as an excitation of this mode. The LSM thus plays a central role in the system's dynamics: Relaxing towards equilibrium it quickly settles onto the LSM and if we pull the system away from equilibrium using a steady forcing pointing almost any direction in phase-space the system will stubbornly respond along its preferred direction.

3 A two-box energy balance model

Having established the shape and time-scale of the least stable mode as being central for the behavior of the climate system, it becomes interesting to determine the physical mechanisms behind these quantities. To this end, we construct a simple two-box energy balance model (EBM) containing the necessary processes to display a behavior similar to that of the GCM. This model may be dealt with analytically and the parameters determining that behavior may be identified.

3.1 Model description

The model consists of a single hemisphere with two boxes divided by the 30th latitude. This choice yields similar surface areas of the two boxes and when choosing

equal mixed layer depths the heat capacity of the low- and high-latitude oceans are also equal. Figure 1 provides a sketch of the model: Each box is characterized by a surface (mixed layer) temperature which is influenced by the net downwelling shortwave radiation at the top-of-atmosphere (TOA), S_i, the outgoing longwave radiation (OLR) and the meridional heat transport. The OLR is parameterized in the usual Budyko-Sellers (e.g., Budyko, 1969; Sellers, 1969; North, 1975) fashion as, $A + BT_i$, where B gives the sensitivity of the OLR to surface temperature changes and A is a tunable parameter. For reasons that will be discussed in depth later, a value of $B = 0.1PW/K$ is chosen (PW is $10^{15}W$). This corresponds to the rather low TOA sensitivity of about 0.8 $Wm^{-2}K^{-1}$ in the units typically used for B. Albedo variations are neglected and the shortwave fluxes are thus kept constant. The tendency on the surface temperatures are given as the residual of the above fluxes:

$$\dot{T}_1 = \frac{1}{\pi a^2 \rho c_w H}(S_1 - A - BT_1 - F) \tag{11}$$

$$\dot{T}_2 = \frac{1}{\pi a^2 \rho c_w H}(S_2 - A - BT_2 + F), \tag{12}$$

where a is the radius of the Earth and πa^2 thus yields half the area of a hemisphere. Values of S_1, S_2, and A are tuned to give the specified equilibrium $(\bar{T}_1, \bar{T}_2) = (298, 278)K$, and we consider only deviations from this equilibrium, $T_i' = T_i - \bar{T}_i$. The meridional heat transport, F, is parameterized linearly in terms of the meridional temperature gradient and the low-latitude temperature:

$$F = \bar{F} + (T_1' - T_2')\gamma_1 + T_1'\gamma_2. \tag{13}$$

The first term is the equilibrium transport, which is tuned along with S_1, S_2, and A. The second term proportional to the temperature gradient is to mimic the increase in transport with increasing baroclinicity and is the one normally included in EBMs. The last term proportional only to T_1' is included to mimic the effect of an

increased moisture supply and thus greater latent heat transport with increased low- to mid-latitude temperatures. In Figure 10(c) in Alexeev et al. (2005), we showed the resulting meridional heat transport changes from three different fixed SST experiments with the aquaplanet CCM3: a 1 K low-latitude temperature increase relative to equilibrium, a 1 K high-latitude increase and a global 1 K increase. The maximum change in the three experiments was approximately 0.3, -0.15 and 0.15 PW and we have accordingly chosen the sensitivities[1]

$$\gamma_1 = \gamma_2 = 0.15 PW/K, \tag{14}$$

as the basic parameter setting in the following. In the three Alexeev et al. (2005) fixed SST experiments we thus get

$$\begin{aligned}
\text{low:} \quad & T_1' - T_2' = 1K,\ T_1' = 1K \qquad F' = 2(1K \cdot 0.15PW/K) = 0.3PW \\
\text{high:} \quad & T_1' - T_2' = -1K,\ T_1' = 0K \qquad F' = -1K \cdot 0.15PW/K = -0.15PW \\
\text{glob:} \quad & T_1' - T_2' = 0K,\ T_1' = 1K \qquad F' = 1K \cdot 0.15PW/K = 0.15PW.
\end{aligned}$$

With these parameterizations the system can be written in matrix form as

$$\begin{pmatrix} \dot{T}_1' \\ \dot{T}_2' \end{pmatrix} = \frac{1}{C} \begin{pmatrix} -B - \gamma_1 - \gamma_2 & \gamma_1 \\ \gamma_1 + \gamma_2 & -B - \gamma_1 \end{pmatrix} \begin{pmatrix} T_1' \\ T_2' \end{pmatrix} \tag{15}$$

where $C = \pi a^2 \rho c_w H$ is the heat capacity of each of the boxes. Since γ_1, γ_2 and B are all positive, both diagonal entries in the Jacobian are negative and thus tend to remove perturbations. The off-diagonal entries are both positive and tend to communicate a perturbation from one box to the other.

The parameterization, eqn. (13), for the meridional energy transport is obviously

[1]These are round numbers only. The changes in the low-latitude, high-latitude and uniform SST change experiments could also be read off as 0.3, -0.2 and 0.1 PW, respectively. In that case we would arrive at $(\gamma_1, \gamma_2) = (0.2, 0.1)PW/K$. Since this has no impact on the qualitative conclusions reached in the following, we have chosen to use the parameter setting where the γ's are equal.

only one out of several possibilities. For the last term in the parameterization in eqn. (13) one might have chosen the global mean temperature rather than simply the low-latitude temperature, and we have done this without showing the result. The values of the parameters γ_1 and γ_2 change and the algebra in what follows is slightly different, but the qualitative conclusions remain unchanged. We have chosen the low-latitude temperature both because this is physically more important for the atmospheric moisture supply and because the algebra is especially simple with this choice. Another parameterization which perhaps is more physically based and consistent with the results of Caballero and Langen (2005) would be one where the extra low-latitude contribution is scaled with the temperature gradient, since it is the same baroclinic eddy motions that are responsible for both contributions:

$$F = (T_1 - T_2)\gamma_1 + (T_1 - T_2)\gamma_1 T_1 \gamma_2 = (T_1 - T_2)\gamma_1(1 + \gamma_2 T_1).$$

However, when we linearize about the model's equilibrium (since we are here concerned with small perturbations), this yields the perturbation transport

$$F' = [\gamma_1(1 + \gamma_2 \bar{T}_1) + \gamma_1\gamma_2(\bar{T}_1 - \bar{T}_2)]T_1' - [\gamma_1(1 + \gamma_2 \bar{T}_1)]T_2',$$

and we are left in a situation where $\gamma_2 \neq 0$ leads to an added positive sensitivity to T_1' relative to the negative sensitivity to T_2'. This added sensitivity is equivalent to $\gamma_2 \neq 0$ in eqn. (13), and is what in the following will be demonstrated to play the decisive role for polar amplification. When linearized, the different possible parameterizations taking the moisture supply effect into account are thus equivalent. The latter non-linear parameterization would, however, change the model's behavior were the linearization dropped and larger perturbations considered.

3.2 Eigenmode analysis

As for the Jacobian, $\boldsymbol{\mathcal{R}}$, of the GCM earlier, we determine the eigenmodes of the EBM. The fast mode (subscript "f") has the eigenvalue

$$\lambda_f = -\frac{B + 2\gamma_1 + \gamma_2}{C} \tag{16}$$

corresponding to the decay time-scale

$$\tau_f = \frac{C}{B + 2\gamma_1 + \gamma_2} \tag{17}$$

and the eigenvector

$$\mathbf{v}_f = \begin{pmatrix} 1 \\ -1 \end{pmatrix}. \tag{18}$$

The slow mode (subscript "s") mode – or least stable mode – is

$$\lambda_s = -\frac{B}{C}, \quad \tau_s = \frac{C}{B} \tag{19}$$

$$\mathbf{v}_s = \begin{pmatrix} 1 \\ 1 + \frac{\gamma_2}{\gamma_1} \end{pmatrix}. \tag{20}$$

The fast mode is with its $(1, -1)$ structure one of redistribution of energy between the boxes. Motion in phase space along this vector is simply an increase in temperature in one zone and an equal decrease in the other. The slow mode has the same sign in both zones and therefore corresponds to either global cooling or warming. Its shape is, when γ_1 and γ_2 are approximately equal, polar amplified with a high- to low-latitude ratio of about 2 (and 1.5 if $(\gamma_1, \gamma_2) = (0.2, 0.1)PW/K$). The time-scale of the LSM is set by C and B, i.e., by the heat capacity of the system and by the rate at which extra energy can be lost to space. In the standard parameter setting, where $B = 0.1PW/K$, the time-scale is approximately 100 months. This is the time-scale we find from the GCM relaxation experiment in Section 4 and lies

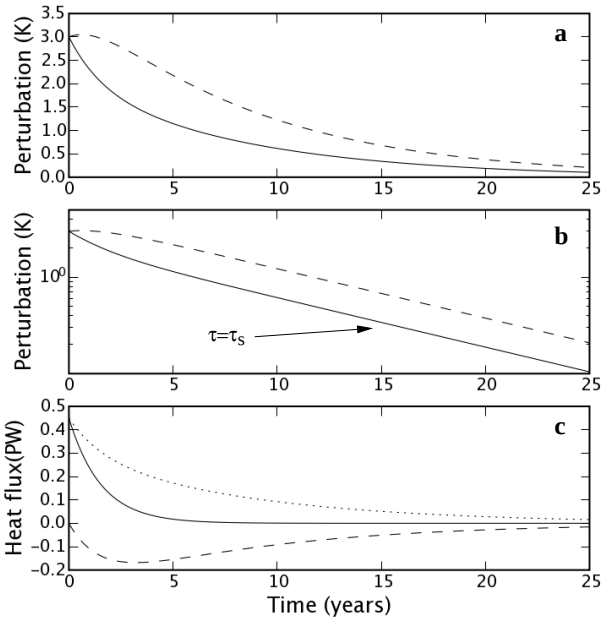

Figure 2: A box model relaxation experiment from an initial 3 K perturbation in both zones. (a) Temperature perturbation in box 1 (solid) and 2 (dashed). (b) As panel (a) but with logarithmic temperature axis. The straight lines that the curves converge to have a slope corresponding to the decay time-scale of the least stable mode. (c) The total heat transport perturbation (solid) broken down into contributions from $(T_1' - T_2')\gamma_1$ (dashed) and $T_1'\gamma_2$ (dotted).

between the two different GCM times-scales evaluated with the perturbation and FDT methods (Alexeev, 2003; Langen and Alexeev, 2005).

The separation in time-scales of the two modes is determined by the magnitude of B compared to the γ's; in the standard parameter setting where the γ's are $0.15PW/K$, the slow time-scale is 5.5 times longer than the fast one (and 6 times longer if $(\gamma_1, \gamma_2) = (0.2, 0.1)PW/K$). If $B = \gamma_1 = \gamma_2$, the separation is 4 times and if B was chosen corresponding to the normal 2 $Wm^{-2}K^{-1}$, the separation would be approximately 3.

3.3 Relaxation to equilibrium

In Figure 2 is shown the result of letting the system relax back to equilibrium from a globally uniform 3 K initial perturbation. Panel (a) shows how the system spends

the first 5 years setting up the LSM polar amplified shape under the influence of the fast mode. In panel (b) it is obvious from the straight lines in the semi-logarithmic plot how the decay thereafter is exponential with decay time-scale τ_s in both zones. At this point, the trajectory is described by the LSM term in the expansion of eqn. (6):

$$\mathbf{T}'_s(t) \sim \mathbf{v}_s e^{\lambda_s t}. \tag{21}$$

It is apparent from eqn. (20) that with positive γ's the least stable mode will always be polar amplified to some degree, which in turn is set by the ratio of the γ's. When the system is dominated by the least stable mode, $T'_2 = (1 + \gamma_2/\gamma_1)T'_1$ and the perturbation in the heat transport vanishes:

$$\begin{aligned} F' &= (T'_1 - T'_2)\gamma_1 + T'_1\gamma_2 = (1 - (1 + \gamma_2/\gamma_1))\gamma_1 T'_1 + \gamma_2 T'_1 \\ &= 0. \end{aligned} \tag{22}$$

This is clearly seen in Figure 2(c) where, after the decay of the fast mode, the two terms contributing to the heat transport exactly cancel out to remove the heat transport perturbation long before the temperature perturbation is damped out. This does, however, not fully explain the least stable mode in physical terms. Such an explanation becomes more apparent when the system is rewritten in terms of the temperature gradient, $\Delta T = T_1 - T_2$, and the global mean temperature, $T_m = (T_1 + T_2)/2$:

$$\begin{pmatrix} \Delta\dot{T}' \\ \dot{T}'_m \end{pmatrix} = \frac{1}{C} \begin{pmatrix} -(B + 2\gamma_1 + \gamma_2) & -2\gamma_2 \\ 0 & -B \end{pmatrix} \begin{pmatrix} \Delta T' \\ T'_m \end{pmatrix}. \tag{23}$$

Here we realize that the state of the gradient has no effect on the evolution of the global mean temperature but that a positive perturbation in the mean temperature tends to decrease the gradient by increasing the heat transport. The above may be

split into two terms,

$$\begin{pmatrix} \Delta\dot{T}' \\ \dot{T}'_m \end{pmatrix} = \underbrace{-\frac{B}{C}\begin{pmatrix} \Delta T' \\ T'_m \end{pmatrix}}_{\text{Slow decay}} + \underbrace{\frac{1}{C}\begin{pmatrix} -(2\gamma_1+\gamma_2) & -2\gamma_2 \\ 0 & 0 \end{pmatrix}\begin{pmatrix} \Delta T' \\ T'_m \end{pmatrix}}_{\text{Fast adjustment of } \Delta T'}, \tag{24}$$

from which it is obvious that the decay is composed of a fast adjustment of the gradient superimposed on a slower decay of both the gradient and the mean temperature controlled by the OLR sensitivity, B. Existence of a positive perturbation in the mean temperature leads to a negative tendency on the gradient due to the latent heat flux term (γ_2). Conversely, a negative perturbation in the gradient leads to a positive tendency. When the gradient is small, the former dominates, and when it is large the latter dominates. Consequently, the system will quickly approach a state where these tendencies cancel,

$$\Delta T \sim -\frac{2\gamma_2}{2\gamma_1+\gamma_2} T_m, \tag{25}$$

and this is exactly the LSM in this representation of the system. Hence, while the global mean temperature decays exponentially from the very beginning of the experiment, the fast mode (redistributing energy between the boxes) quickly adjusts the gradient to match the current mean temperature such that the heat transport perturbation vanishes.

3.4 Response to steady forcing

To determine what happens in a climate change experiment rather than just a relaxation experiment, we return to eqn. (15). We simply insert a steady forcing on the right hand side as an extra contribution to the tendency which in turn is set

equal to zero to achieve the new equilibrium:

$$\frac{1}{C}\begin{pmatrix} -B-\gamma_1-\gamma_2 & \gamma_1 \\ \gamma_1+\gamma_2 & -B-\gamma_1 \end{pmatrix}\begin{pmatrix} \delta T_1 \\ \delta T_2 \end{pmatrix}+\begin{pmatrix} \delta b \\ \delta b \end{pmatrix}=\mathbf{0}, \tag{26}$$

where the δT's are the climate change resulting from the forcing, δb. This solves to

$$\begin{pmatrix} \delta T_1 \\ \delta T_2 \end{pmatrix}=\frac{\delta b}{B(B+2\gamma_1+\gamma_2)}\begin{pmatrix} B+2\gamma_1 \\ B+2\gamma_1+2\gamma_2 \end{pmatrix}. \tag{27}$$

The global mean climate change is simply $\delta b/B$ and thus independent of the heat transport parameters. This parallels the relaxation experiment where global mean temperature was only influenced by B. The ratio between high- and low-latitude warming is

$$\frac{\delta T_2}{\delta T_1} \quad = \quad \left(1+\frac{\gamma_2}{\gamma_1}\right)-\frac{\gamma_2 B}{\gamma_1 B+2\gamma_1^2} \tag{28}$$

where the second term becomes negligible if B is much smaller than the γ's, corresponding to a large separation in time-scales. As demonstrated in eqn. (10), the climate change thus tends to the shape of the LSM as the separation in time-scales increases. In the "dry-atmosphere" case where γ_2 vanishes, a climate change along the LSM is in this model thus uniform between low and high latitudes. This contrasts the results of Cai (2006) who found polar amplification in a box model even without latent heat transports. In that model, atmospheric and surface temperatures are modeled separately and the heat transport is parameterized in terms of the atmospheric temperatures rather than the surface temperatures as done here. A uniform change in the atmospheric emissivity leads in Cai's model to an increased atmospheric equator-to-pole gradient accompanied by an increase in the poleward heat transport and a reduced surface temperature gradient.

4 GCM results

To assess whether the behavior of our EBM carries over to the GCM, we have performed a similar relaxation experiment. It turns out, however, that one single realization of the experiment is too noisy to determine decay rates, TOA fluxes and heat transports sufficiently well. We therefore used a 20 member ensemble of runs with only slightly different initial conditions: In each surface point we added a perturbation relative to the equilibrium SST taken from a Gaussian distribution with mean 3 K and standard deviation 0.15 K. Figure 3(a) shows the result of this experiment: The thin black curves show the individual ensemble member high- and low-latitude temperatures (upper cluster is high-latitude, lower cluster is low-latitude) while the thick white curves show the ensemble means. For each ensemble member (and thus also the ensemble mean), averages have been taken between the two hemispheres. Panel (b) shows the same curves in a semi-logarithmic plot.

4.1 Time scales

Firstly, we compare panels (a) and (b) of Figures 2 and 3. In both cases, the low-latitude temperature drops off rapidly with the high-latitude temperature decaying more slowly. The straight lines in panel (b) of the EBM case carry over reasonably to the GCM case. Especially the high-latitude temperature seems to cool off exponentially, while the low-latitude cooling is somewhat more noisy. It does seem, however, that after the initial 5 to 10 years, the two curves follow straight lines with similar slopes.

To check this in detail, we show in Figure 3(c) the 2-year running mean of the slope of the white curves in panel (b). In the ideal case (like the EBM) these slopes should after the decay of all but the slowest mode be constant and equal to the decay rate of the LSM, i.e., equal to the eigenvalue of the LSM. The slope is very nicely constant and equal to the value -0.01 month^{-1} (corresponding to $\tau_s = 100$ months) for the high-latitude temperature. The slope of the low-latitude temperature is less

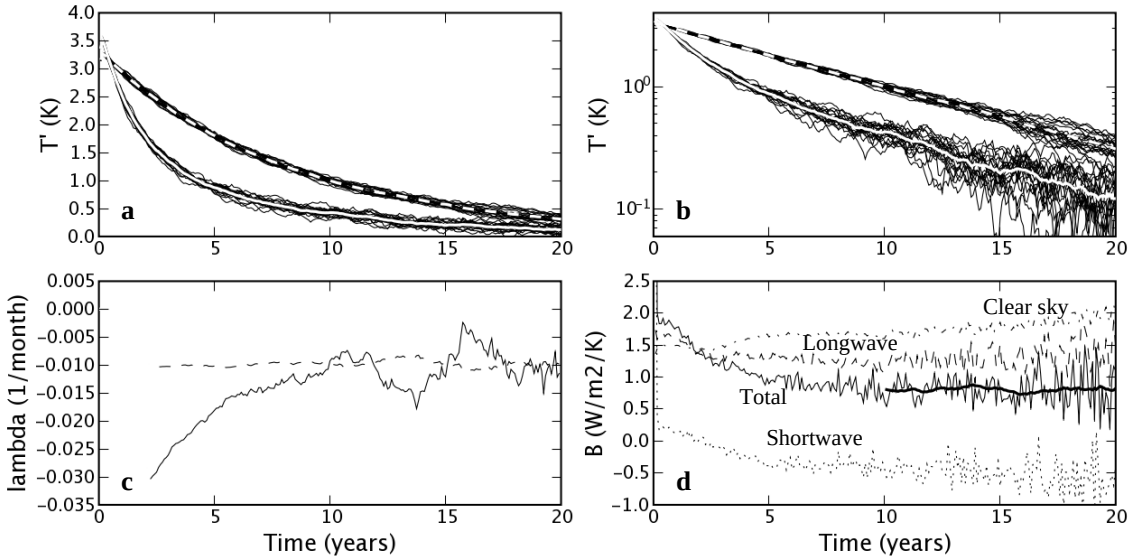

Figure 3: Results of a 20 member GCM ensemble relaxation experiment with an initial 3 K global temperature perturbation. Results for each member have been averaged between the hemispheres. (a) Individual tropical (equatorward of 30 latitude) and extra-tropical (poleward of 30 latitude) ensemble member temperatures (black) and ensemble average tropical (solid white) and extra-tropical (dashed white) temperature. (b) As in panel (a) but with logarithmic temperature axis. (c) Running 2-year average of slope of ensemble average tropical (solid) and extra-tropical (dashed) temperature curves in panel (b). (d) Ensemble and global average TOA change in net upward radiation divided by global average surface temperature change (solid), and longwave (dashed) and shortwave (dotted) contributions thereto. The thick solid line is a running 2-year average. Also shown is the total clear sky counterpart (dash-dotted).

constant (as is also apparent in panel (b)), but it does fluctuate around the value -0.01 month^{-1}. We therefore conclude that, after the decay of faster modes, the system does, in fact, cool off exponentially with the same time-scale in all zones, namely that of the LSM. The 100 month time-scale is reasonably close to the 90 months found in Langen and Alexeev (2005) and the 125 months found when the perturbation method of Alexeev (2003) is used on the present model. The shape of the LSM is from these plots clearly one of higher temperatures at high latitudes.

The time-scale of the LSM was for the EBM found to be determined by the sensitivity of the OLR to surface temperature changes, B. In other words, the slowest decay was concluded to be set by the system's ability to communicate a perturbation to space. Since albedo was held fixed in the EBM, only the longwave sensitivity influenced this communication. In the GCM, however, clouds and water vapor content can change and the shortwave sensitivity must also be taken into account. Furthermore, considering the TOA sensitivity along with SST decay rates is warranted under the assumptions made in the derivation of the linear theory, since, on global average, the imbalance is independent of level when the atmosphere is in equilibrium with the current state of the surface (on time-scales longer than that of the atmosphere). Figure 3(d) thus displays the global average net upward radiation change divided by the global average SST change (solid line). The thick solid line shows a running 2-year average, while the dashed and dotted lines show the long- and shortwave contributions, respectively. After the faster modes have decayed, the total flux sensitivity is rather constant at a value of about 0.8 $Wm^{-2}K^{-1}$ which comes about as the sum of about 1.3 and -0.5 $Wm^{-2}K^{-1}$ from the long- and shortwave. This value of 0.8 $Wm^{-2}K^{-1}$ yields exactly the decay time-scale of 100 months.

We chose the same value for the EBM although it is quite a bit lower than the typical value of about 2 $Wm^{-2}K^{-1}$ used in EBMs. This was mainly done to have time-scales in the EBM closer to those in the GCM. The key point is that in both the EBM and the GCM the final decay rate of the system is controlled by the

TOA radiation sensitivity. In our case, this decay is delayed somewhat compared to typical EBMs and the dash-dotted curve in Figure 3(d) gives us a hint as to why: The clear-sky sensitivity, evaluated in the model by an offline pass to the radiation code ignoring effects of clouds, is much closer to 2 $Wm^{-2}K^{-1}$. Hence, clouds have a warming effect when the system is dominated by the LSM and thus tend to delay the relaxation. We will return to this cloud effect in the next subsection.

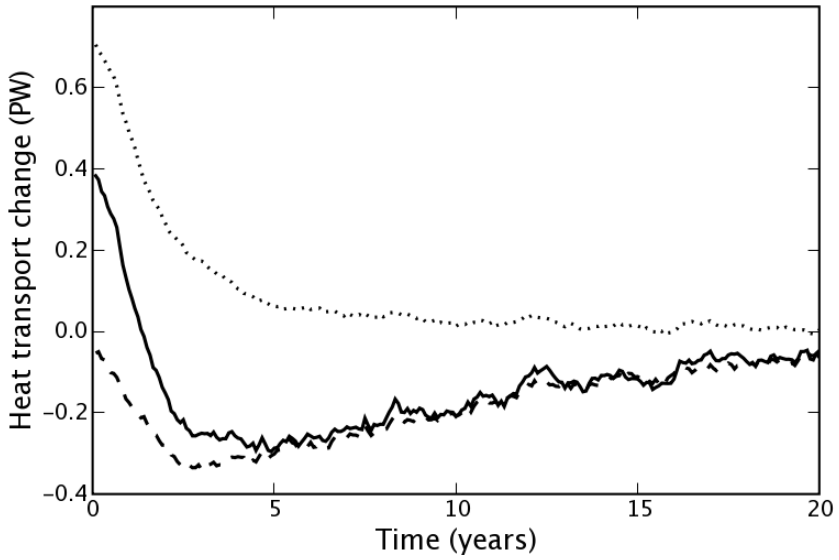

Figure 4: Ensemble average maximum heat transport change during the GCM relaxation experiments (solid) and the maximum dry static energy (dashed) and latent heat (dotted) transport changes.

Figure 4 shows the evolution of the maximum poleward atmospheric heat transports during the experiment. The solid line is the maximum total transport, while the dotted and dashed lines are the maximum latent and dry static energy transport changes. As in the EBM (see Figure 2(c)), the total transport adjusts rapidly during the decay of the faster modes. This happens as a result of both a decrease in the latent heat transport and in the dry static energy transport (due to the low-latitude cooling and decrease in temperature gradient). Unlike in the EBM, the total transport change does not vanish once the system reaches the LSM. Rather, a negative change is observed. This has to do with the changes in the cloud radiative forcing

that also worked to slow down the decay: as will be demonstrated in the next subsection, the cloud radiative forcing is negative at low latitudes and positive at high latitudes. This corresponds to a positive poleward heat transport which must be canceled out by a negative actual heat transport.

4.2 The least stable mode

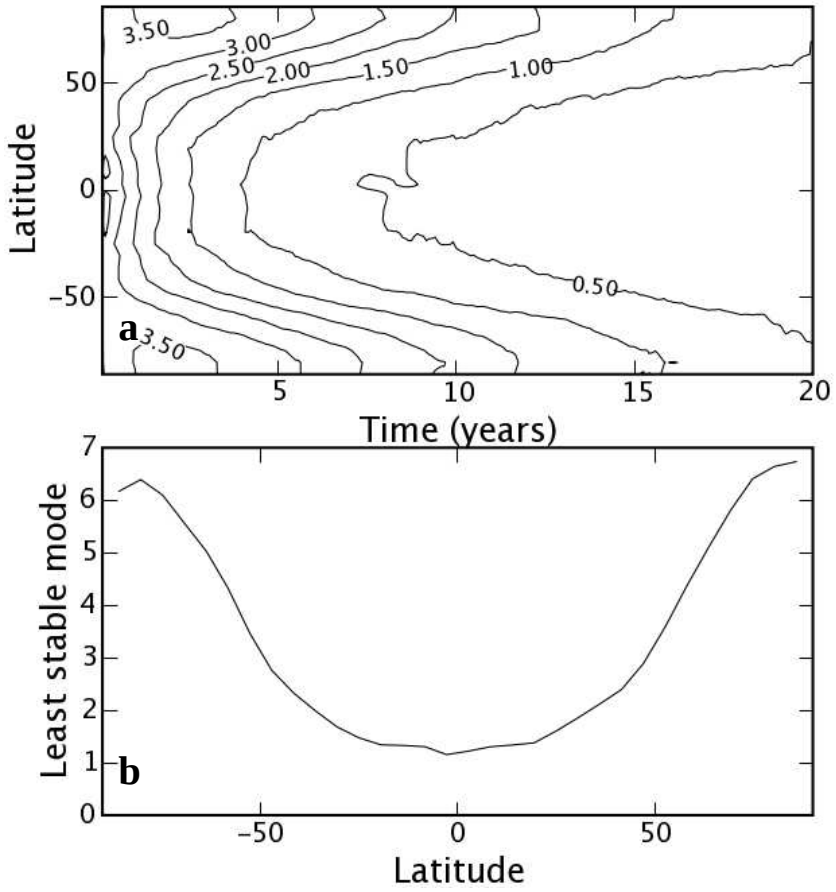

Figure 5: (a) Ensemble and zonal average surface temperature perturbation during relaxation experiment. (b) Least stable mode of the model climate system as evaluated from the latter 10 years of the relaxation experiment.

In this section we will demonstrate a way of evaluating the shape of the LSM from the relaxation experiment. We will also use the method to determine the associated changes in other climate fields. Figure 5(a) shows the ensemble and zonal average

surface temperatures during the relaxation experiment. Initially, the high-latitudes warm while the low latitudes cool. Eventually the system reaches the shape of the least stable mode and the figure displays the characteristic horse-shoe pattern. As mentioned earlier, when the faster modes have decayed, the remaining temperature perturbation is given by

$$\mathbf{T}'_s(t) \sim \mathbf{v}_s e^{\lambda_s t}. \tag{29}$$

This can be solved for the LSM,

$$\mathbf{v}_s \sim \mathbf{T}'_s(t) e^{-\lambda_s t}, \tag{30}$$

and we can average over the latter part of our experiment,

$$\mathbf{v}_s = \langle \mathbf{T}'_s(t) e^{-\lambda_s t} \rangle_{t=10-20yr}, \tag{31}$$

to extract the shape of the LSM. An eigenvector is only defined to within an arbitrary constant, and with this technique we get the projection of the initial state onto the vector. Figure 5(b) shows the LSM as calculated in this manner, and the shape (and magnitude) is very robust to the choice of averaging period. This LSM is very similar to those found by evaluating $\boldsymbol{\mathcal{R}}$ in eqn. (5) with a perturbation method (Alexeev, 2003) and with the fluctuation-dissipation theorem (Langen and Alexeev, 2005). This technique can, however, be utilized to evaluate not only the LSM in the surface temperature, but also changes in other fields associated therewith. Assuming that, with the rather small climate changes dealt with here, cloud and radiation fields are related linearly with surface temperature changes (basically the same assumption as in Section 2.2), we can rewrite eqn. (31) using, for example, the 2 dimensional (zonally averaged) cloud fraction field,

$$\mathbf{C}_s = \langle \mathbf{C}'_s(t) e^{-\lambda_s t} \rangle_{t=10-20yr}. \tag{32}$$

The result of this calculation is shown in Figure 6(a), where solid contours mark positive changes and dashed contours mark negative changes. Surface temperature changes along the least stable mode lead – in this model – to a decrease and upward shift of the equatorial high clouds, while in mid- to high latitudes we see a decrease in low to medium clouds and a slight increase in high clouds.

These changes in the mean cloud field, and possibly also changes in the cloud variability and cloud water, lead to changes in the TOA radiative fluxes that are most easily expressed with the cloud radiative forcing (CRF). The CRF is the difference between the actual (all-sky including clouds) radiation and the clear-sky radiation and can be evaluated both at the surface and the TOA. We calculate the TOA CRF for longwave, shortwave and total flux according to

$$\begin{aligned} \mathrm{CRF_{SW}} &= F^{\downarrow}_{SW} - F^{\downarrow}_{SW,\mathrm{clear}} \\ \mathrm{CRF_{LW}} &= F^{\downarrow}_{LW} - F^{\downarrow}_{LW,\mathrm{clear}} \\ \mathrm{CRF} &= \mathrm{CRF_{SW}} + \mathrm{CRF_{LW}}, \end{aligned}$$

and use these quantities in calculations parallel to those of eqs. (31) and (32). The result is shown in Figure 6(b) where the solid curve is the total TOA CRF change associated with climate changes along the LSM. The dashed and dotted lines are the long- and shortwave components. Most striking is the positive CRF at mid- to high latitudes which is due to both long- and shortwave contributions. While it is outside the scope of the present study to determine exactly how the CRF is formed, we might tentatively ascribe the former to the increase in high clouds and the latter to the decrease in low to medium clouds (again, cloud water and variability changes may also play a role). At the equator, the decrease in high cloud seemingly leads to a decrease in the longwave CRF.

These CRF changes relate directly to two issues discussed earlier: (i) The overall positive CRF is responsible for delaying the relaxation in the GCM by decreasing the radiative sensitivity to 0.8 $Wm^{-2}K^{-1}$ (cf. Figure 3(d)). In fact, the global

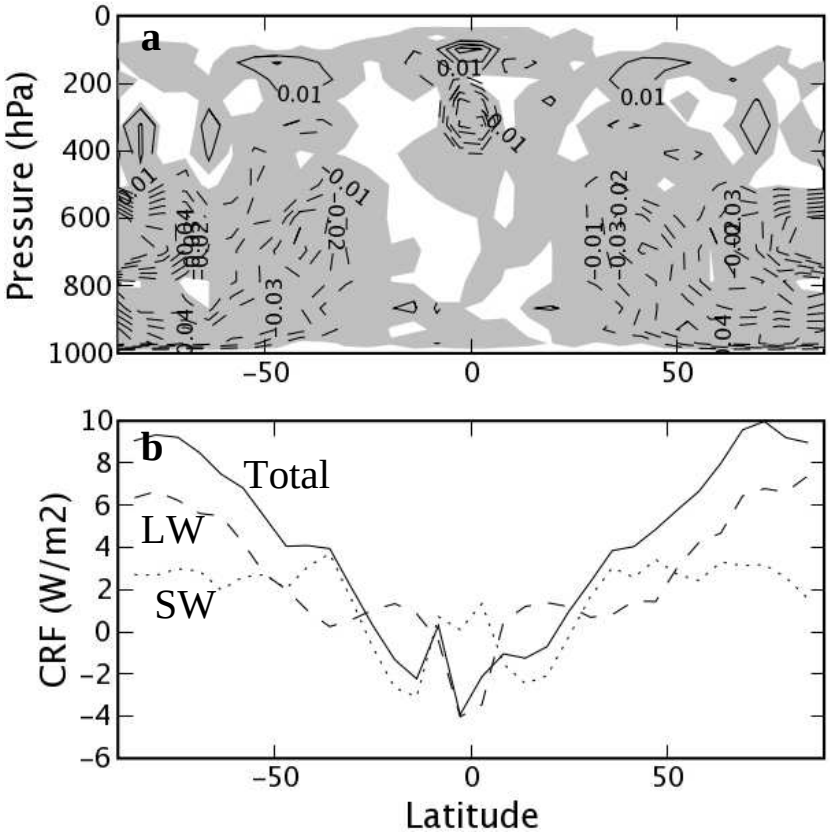

Figure 6: Ensemble and zonal average cloud quantity changes associated with surface temperature perturbations along the least stable mode. Evaluated in same manner as least stable mode in Figure 5(b). (a) Cloud fraction. Dashed contours signify negative changes. Grey shading marks areas where changes are significant at the 95% level estimated using the t-test on the 20 ensemble members. The changes in the members are assumed independent and Gaussian. (b) Total TOA cloud radiative forcing change (solid), and longwave (dashed), shortwave (dotted) contributions thereto.

average of the total CRF change divided by the global average of the LSM equals approximately 1 $Wm^{-2}K^{-1}$, which added to the all-sky sensitivity would bring us close to the typical EBM value of 2 $Wm^{-2}K^{-1}$. Since CRF changes are not equivalent to cloud feedback (Soden et al., 2004), this should not, however, be seen as an attempt to estimate feedback. It is rather an identification of the cloud contribution to TOA radiation change when the system is governed by the LSM. However, due to the inherent differences between the model types, we should not expect to be able to completely reconcile the sensitivities of the GCM and the EBM. For instance, many feedbacks (such as the lapse rate feedback) alter the geographical distribution of sensitivity (Colman, 2002) and may thus influence global sensitivity. (ii) As discussed by Weaver (2003), there is a close relationship between the gradient of CRF and atmospheric and oceanic energy transports. In the present case, the pattern of negative change at low latitudes and positive change at high latitudes has the same effect on the TOA radiation imbalance as a positive atmospheric heat transport. This yields a positive tendency on ΔT and, according to the discussion following eqn. (24), the temperature profile must adjust such as to balance the two heat transport contributions and the positive cloud contribution. This leads to the negative heat transport change in Figure 4.

5 Conclusions

Through a combination of theoretical considerations related to the climate system's linearized surface budget, a simple EBM and an ensemble experiment with a GCM, we have explored the notion of polar amplification being an excitation of the climate system's least stable mode. When the system is perturbed, it relaxes back to equilibrium along the least stable mode. Prior to this, faster modes act to redistribute heat within the system to set up the characteristic polar amplified shape of the least stable mode. On the least stable mode, the meridional temperature gradient is exactly such as to counter the increase in atmospheric heat transport set

up by the low-latitude temperature perturbation (and in the GCM case, the heat transport implied by cloud radiative forcing changes). From the EBM analysis it became apparent that this was necessary due to the heat transport processes being faster than the final decay.

The fast time-scale is thus one of redistribution of energy in the system while the slowest is one of energy-loss to space. In fact, the degree to which the LSM becomes visible during the decay is determined by the separation between these time-scales: a fast redistribution of heat will quickly collapse the system onto the LSM while a small separation will allow non-LSM components to survive. In a climate change experiment, where the system responds to a steady forcing, the time-scale separation also determines how cleanly the LSM is excited.

It is worth stressing that the shape of the LSM is set by the fast atmospheric dynamics and studies considering an equilibrium response or the slow evolution accompanying a gradual increase in forcing may overlook the underlying mechanisms for the polar amplification. This agrees well with the recent work of Graversen (2006) who found only a small part of the observed recent polar amplified warming trend to be associated with increase in poleward atmospheric heat transport. It is also consistent with the near cancellation in the new equilibrium between dry static energy and latent heat transport changes found in the CO_2-doubling experiment by Boer (1995).

The decay time-scale of the LSM, and thereby also the time-scale for removal of a perturbation to the system, is rather intuitively determined by the rate at which energy can be lost to space. Within the EBM framework, it is not influenced by the heat transport parameters, which only set the shape of the LSM. In the GCM, however, there is the caveat that cloud effects were found to delay the communication with space relative to the clear-sky and classical EBM value. Assuming that these cloud effects are affected by the shape of the LSM, which in turn is affected by the heat transport, the decay time-scale is in the GCM indirectly influenced by the heat transport sensitivity.

The shape of the LSM is determined by the ratio of heat transport sensitivity to low-latitude temperature changes and gradient changes (cf. eqn. (20)). If γ_2 vanishes, the least stable mode would no longer be polar amplified but rather just a constant vector. Climate changes along this mode are thus more uniform with similar changes in low and high latitudes. Caballero and Langen (2005) found a warm low-gradient regime ($(\Delta T, T_m) \simeq (20, 20)$°C) to exist in which the total atmospheric heat transport no longer depends on global mean temperature changes but only on gradient changes. If true, this would imply that climate changes during, for example, the Eocene would be more uniform than polar amplified. This conclusion is particularly interesting in light of the recent findings of Sluijs et al. (2006) where a Palaeogene polar marine sedimentary core from hole 302-4A of the Integrated Ocean Drilling Program is analyzed. They find that the Palaeocene/Eocene thermal maximum – a warm event during the warm, low-gradient early Palaeogene background climate – experienced warming near the North Pole of about 5°C. This is not polar amplified relative to the approximately 4–8°C warming documented at low to mid-latitudes.

The present study is a continuation of our earlier work, and we have studied the relationship between the relaxation of perturbations, the LSM and polar amplification. The success of the perturbation method (Alexeev, 2003) and the FDT method (Langen and Alexeev, 2005) in predicting the response to an external forcing shows that the linear theory employed here is valid – at least for small perturbations and forcings: when other climate regimes are considered as above, the Jacobian of the system must be re-evaluated. With the exponential decay of temperature perturbations seen in Figure 3, we thus find the projection of the GCM response onto this decay a reasonable way to determine the LSM (in SSTs) and the associated changes in other fields. In fact, this projection-method may even prove to be the most practical one for determining the LSM in non-aquaplanet configurations where the above methods seem less applicable due to the higher phase-space dimensionality and necessary averaging times introduced by the non-zonality in the model

statistics.

6 Acknowledgments

This research is supported by the Carlsberg Foundation and National Science Foundation Agreement No. ARC-0327664. This work was supported in part by a grant of HPC resources from the Arctic Region Supercomputing Center at the University of Alaska Fairbanks as part of the Department of Defense High Performance Computing Modernization Program. The suggestions by two anonymous reviewers substantially improved both the content and the clarity of the manuscript.

References

ACIA (2004). *Impacts of a warming Arctic: Arctic Climate Impact Assessment*. Cambridge University Press.

Alexeev, V. A. (2003). Sensitivity to CO_2 doubling of an atmospheric GCM coupled to an oceanic mixed layer: a linear analysis. *Clim. Dyn.*, 20:775–787.

Alexeev, V. A., Langen, P. L., and Bates, J. R. (2005). Polar amplification of surface warming on an aquaplanet in "ghost forcing" experiments without sea ice feedbacks. *Clim. Dyn.*, doi:10.1007/s00382-005-0018-3.

Arrhenius, S. (1896). On the influence of carbonic acid in the air upon the temperature of the ground. *Phil. Mag.*, 41:237–276.

Boer, G. J. (1995). Some dynamical consequences of greenhouse gas warming. *Atmos.-Oc.*, 33:731–751.

Budyko, M. (1969). The effect of solar radiation variations on the climate of the Earth. *Tellus*, 21(5):611–619.

Caballero, R. and Langen, P. L. (2005). The dynamic range of poleward energy transport in an atmospheric general circulation model. *Geophys. Res. Lett.*, 32:L02705, doi:10.1029/2004GL021581.

Cai, M. (2005). Dynamical amplification of polar warming. *Geophys. Res. Lett.*, 32:L22710, doi:10.1029/2005GL024481.

Cai, M. (2006). Dynamical greenhouse-plus feedback and polar warming amplification. Part I: A dry radiative-transportive climate model. *Clim. Dyn.*, 26:661–675.

Colman, R. (2002). Geographical contributions to global climate sensitivity in a general circulation model. *Global and Planetary Change*, 32:211–243.

Graversen, R. G. (2006). Do changes in the midlatitude circulation have any impact on the Arctic surface air temperature trend? *J. Climate*, 19:5422–5438.

Hall, A. (2004). The role of surface albedo feedback in climate. *J. Climate*, 17:1550–1568.

Hall, A. and Qu, X. (2006). Using the current seasonal cycle to constrain snow albedo feedback in future climate change. *Geophys. Res. Lett.*, 33:L03502,doi:10.1029/2005GL025127.

Hansen, J., Sato, M., Ruedy, R., Nazarenko, L., Lacis, A., Schmidt, G. A., Russell, G., Aleinov, I., Bauer, M., Bauer, S., Bell, N., Cairns, B., Canuto, V., Chandler, M., Cheng, Y., Del Genio, A., Faluvegi, G., Fleming, E., Friend, A., Hall, T., Jackman, C., Kelley, M., Kiang, N., Koch, D., Lean, J., Lerner, J., Lo, K., Menon, S., Miller, R., Minnis, P., Novakov, T., Oinas, V., Perlwitz, J., Perlwitz, J., Rind, D., Romanou, A., Shindell, D., Stone, P., Sun, S., Tausnev, N., Thresher, D., Wielicki, B., Wong, T., Yao, M., and Zhang, S. (2006). Efficacy of climate forcings. *J. Geophys. Res.*, 110(D18104).

Holland, M. M. and Bitz, C. M. (2003). Polar amplification of climate change in coupled models. *Clim. Dyn.*, 21:221–232.

Hoskins, B. J. and Karoly, D. J. (1981). The steady linear response of a spherical atmosphere to thermal and orographic forcing. *J. Atmos. Sci.*, 38:1179–1196.

Kiehl, J. T., Hack, J. J., Bonan, G. B., Boville, B. A., Briegleb, B. P., Williamson, D. L., and Rasch, P. J. (1996). Description of the NCAR Community Climate Model (CCM3). Technical Report TN-420, CGD, National Center for Atmospheric Research.

Langen, P. L. and Alexeev, V. A. (2004). Multiple equilibria and asymmetric climates in the CCM3 coupled to an oceanic mixed layer with thermodynamic sea ice. *Geophys. Res. Lett.*, 31:doi: 10.1029/2003GL019039.

Langen, P. L. and Alexeev, V. A. (2005). Estimating $2\times CO_2$ warming in an aquaplanet GCM using the fluctuation-dissipation theorem. *Geophys. Res. Lett.*, 32:doi: 10.1029/2005GL024136.

Manabe, S. and Wetherald, R. T. (1980). On the distribution of climate change resulting from an increase in the CO_2 content of the atmosphere. *J. Atmos. Sci.*, 37:99–118.

Masson-Delmotte, V., Kageyama, M., Braconnot, P., Charbit, S., Krinner, G., Ritz, C., Guilyardi, E., Jouzel, J., Abe-Ouchi, A., Crucifix, M., Gladstone, R. M., Hewitt, C. D., Kitoh, A., LeGrande, A. N., Marti, O., Merkel, U., Motoi, T., Ohgaito, R., Otto-Bliesner, B., Peltier, W. R., Ross, I., Valdes, P. J., Vettoretti, G., Weber, S. L., Wolk, F., and Yu, Y. (2006). Past and future polar amplification of climate change: climate model intercomparisons and ice-core constraints. *Clim. Dyn.*, 26:513–529.

North, G. R. (1975). Theory of energy-balance climate models. *J. Atmos. Sci.*, 32:2033–2043.

Qu, X. and Hall, A. (2006). Assessing snow albedo feedback in simulated climate change. *J. Climate*, 19:2617–2630.

Rodgers, K. B., Lohmann, G., Lorenz, S., Schneider, R., and Henderson, G. M. (2003). A tropical mechanism for Northern Hemisphere deglaciation. *Geochem. Geophys. Geosys.*, 4(5):1046, doi:10.1029/2003GC000508.

Schneider, E. K., Kirtman, B. P., and Lindzen, R. S. (1999). Tropospheric water vapor and climate sensitivity. *J. Atmos. Sci.*, 56:1649–1658.

Schneider, E. K., Lindzen, R. S., and Kirtman, B. P. (1997). A tropical influence on global climate. *J. Atmos. Sci.*, 54:1349–1358.

Sellers, W. D. (1969). A global climatic model based on the energy balance of the Earth-atmosphere system. *J. Appl. Meteor*, 8:392–400.

Shine, K. P., Cook, J., Highwood, E. J., and Joshi, M. M. (2003). An alternative to radiative forcing for estimating the relative importance of climate change mechanisms. *Geophys. Res. Lett.*, 30(20):2047.

Sluijs, A., Schouten, S., Pagani, M., Woltering, M., Brinkhuis, H., Damsté, J. S. S., Dickens, G. R., Huber, M., Reichart, G.-J., Stein, R., Matthiessen, J., Lourens, L. J., Pedentchouk, N., Backman, J., Moran, K., and the Expedition 302 Scientists (2006). Subtropical Arctic Ocean temperatures during the Palaeocene/Eocene thermal maximum. *Nature*, 441:610–613.

Soden, B. J., Broccoli, A. J., and Hemler, R. S. (2004). On the use of cloud forcing to estimate cloud feedback. *J. Climate*, 17:3661–3665.

Solomon, A. (2006). Impact of latent heat release on polar climate. *Geophys. Res. Lett.*, 33:L07716, doi:10.1029/2005GL025607.

Wallace, J. M. and Gutzler, D. S. (1981). Teleconnections in the geopotential height field during the Northern Hemisphere winter. *Mon. Wea. Rev.*, 109:785–812.

Weaver, C. P. (2003). Efficiency of storm tracks an important climate parameter? The role of cloud radiative forcing in poleward heat transport. *J. Geophys. Res.*, 108.

Winton, M. (2006). Amplified Arctic climate change: What does surface albedo feedback have to do with it? *Geophys. Res. Lett.*, 33:L03701, doi:10.1029/2005GL025244.

Zachos, J. C., Pagani, M., Sloan, L. C., Thomas, E., and Billups, K. (2001). Trends, rhythms and aberrations in global climate 65 Ma to present. *Science*, 292:686–693.